

Probing the Ni(OH)₂ Precursor for LiNiO₂ at the Atomic Scale: Insights into the Origin of Structural Defect in a Layered Cathode Active Material

Anuj Pokle,^{*} Daniel Weber, Matteo Bianchini, Jürgen Janek, and Kerstin Volz

In lithium ion batteries (LIBs), the layered cathode materials of composition LiNi_{1-x-y}Co_xMn_yO₂ are critical for achieving high energy densities. A high nickel content (>80%) provides an attractive balance between high energy density, long lifetime, and low cost. Consequently, Ni-rich layered oxides cathode active materials (CAMs) are in high demand, and the importance of LiNiO₂ (LNO) as limiting case, is hence paramount. However, achieving perfect stoichiometry is a challenge resulting in various structural issues, which successively impact physicochemical properties and result in the capacity fade of LIBs. To better understand defect formation in LNO, the role of the Ni(OH)₂ precursor morphology in the synthesis of LNO requires in-depth investigation. By employing aberration-corrected scanning transmission electron microscopy, electron energy loss spectroscopy, and precession electron diffraction, a direct observation of defects in the Ni(OH)₂ precursor prepared is reported and the *ex situ* structural evolution from the precursor to the end product is monitored. During synthesis, the layered Ni(OH)₂ structure transforms to partially lithiated (non-layered) NiO and finally to layered LNO. The results suggest that the defects observed in commercially relevant CAMs originate to a large extent from the precursors, hence care must be taken in tuning the co-precipitation parameters to synthesize defect-free Ni-rich layered oxides CAMs.

to increasing transition metals prices, especially cobalt (Co). Co is a core material component in commercial cathodes such as LiCoO₂ (LCO), LiNi_{0.6}Co_{0.2}Mn_{0.2}O₂, and LiNi_{0.8}Co_{0.15}Al_{0.05}O₂.^[1-3] Due to its price as well as moral/environmental concerns, Co has become a critical material and efforts have been made to develop Co-free cathodes based on LiNiO₂ (LNO), mostly stabilized by doping.^[1,4] Similar to LCO, LNO provides a high theoretical capacity of up to 274 mAh g⁻¹ and costs lower. This spurs a row of investigations into its crystal chemistry in order to understand the interplay between its atomic structure, microstructure, and specific capacity.^[5,6]

The crystal structure of LNO, defects therein and achievable cathode active material (CAM) performance strongly depend on the synthesis process. The LNO phase consists of a cubic close packed sublattice of oxygen anions, and Li and Ni alternately fill the octahedral interstitial sites along the [111] direction of the cubic lattice. The different steric constraints

imposed by the Ni³⁺ and Li⁺ ions result in a rhombohedral distortion, that is, an *R-3m* space group symmetry.

Critical synthesis parameters are the choice of precursors, temperature profiles, and gas atmosphere. With regards

1. Introduction

Electrification of automobiles has propelled efforts to enhance battery performance but simultaneously faces challenges linked

A. Pokle,^[*] K. Volz
Materials Science Center (WZMW) and Department of Physics
Philipps-University Marburg
35032 Marburg, Germany
E-mail: pokle@staff.uni-marburg.de

 The ORCID identification number(s) for the author(s) of this article can be found under <https://doi.org/10.1002/smll.202205508>.

© 2022 The Authors. Small published by Wiley-VCH GmbH. This is an open access article under the terms of the Creative Commons Attribution-NonCommercial-NoDerivs License, which permits use and distribution in any medium, provided the original work is properly cited, the use is non-commercial and no modifications or adaptations are made.

^[*]Present address: Department of Physics, Center for Materials Science and Nanotechnology (SMN), University of Oslo, 0349 Oslo, Norway

^[**]Present address: Faculty of Biology, Chemistry and Earth Sciences, Bayerisches Zentrum für Batterietechnik (BayBatt), University of Bayreuth, D-95447 Bayreuth, Germany

D. Weber, J. Janek
Battery and Electrochemistry Laboratory
Institute of Nanotechnology
Karlsruhe Institute of Technology (KIT)
Hermann-von-Helmholtz-Platz 1, 76344 Eggenstein-Leopoldshafen,
Germany

M. Bianchini,^[**]
Battery and Electrochemistry Lab (BELLA)
BASF SE
Carl-Bosch-Strasse 38, 67056 Ludwigshafen, Germany

J. Janek
Institute of Physical Chemistry & Center for Materials Research
Justus-Liebig-University
Heinrich-Buff-Ring 17, 35392 Giessen, Germany

DOI: 10.1002/smll.202205508

to cost, the precursor of choice is Ni(OH)₂ precipitated from NiSO₄·H₂O. Ni(OH)₂ is then pre-annealed with LiOH·H₂O at high temperatures. In order to achieve higher energy efficiency during industrial synthesis, the compounds are pre-annealed at medium temperatures of 400–500 °C for dehydration.^[6–8] Subsequently, the dehydrated intermediates are repacked into to new sagger type reactors to achieve a maximum volume efficiency and heated at about 700–750 °C to promote lithiation and crystallization. This results in the end product (LNO) in a secondary particle morphology, forged by lithiation/oxidation of the secondary Ni(OH)₂ particles with LiOH from the precursor LiOH·H₂O.^[5,9]

Even though there are numerous neutron diffraction and X-ray diffraction (XRD) studies on the synthesis process of the Ni-rich layered oxides CAMs, structural investigations on the precursors are scarce.^[5,6,10–18] Since the used techniques are bulk sensitive and spatially averaging, structural defects such as impurities or stacking faults are usually missed. Hence, to understand the influence of defects on the synthesis and in order to further improve CAM synthesis, information on the type of local crystalline defects and their influence on the final product are vital.^[19,20]

To date, much attention has been given to electrochemical cycling-induced crystalline defects in LNO, that is, to the role of chemomechanics. We assume that inherent defects in pristine LNO are equally important but are underexplored.^[5,21–23] In addition to mitigating electrochemical cycling-induced defects, the structural evolution of the precursor material during the synthesis process must be thoroughly studied. Here, high-resolution (HR) electron microscopy can complement the picture by probing local crystalline defects in the precursor material.^[24–27] Aberration-corrected scanning transmission electron microscopy (AC-STEM) is a multifaceted technique to probe the local structure and chemical properties, wherein the high-angle annular dark-field (HAADF) signal is directly proportional to the atomic number ($\approx Z^{1.7}$).^[28,29] Apart from the imaging mode, electron energy loss spectroscopy (EELS) measurement provides elemental composition and bonding information.

Furthermore, the precession electron diffraction (PED) technique can be employed to obtain a quasi-kinematic diffraction pattern that is suitable to explore the reciprocal space.^[30] In this work, we use AC-STEM to access structural information in materials with high surface area, which is not possible to obtain with other spatially averaging methods such as powder XRD (PXRD). The Ni(OH)₂ precursor has been prepared by industrially relevant methods (precipitation), which results in a polycrystalline secondary particle morphology (we refer to the SEM micrographs in Figure S1, Supporting Information). The primary particles are highly compact nanosized Ni(OH)₂ platelets, wherein the structural investigation at high-spatial resolution is impeded by projection and e-beam induced effects.

In the following, we explore the structural and compositional evolution of the Ni(OH)₂ precursor, through an intermediate NiO-like (Ni_{1-y}Li_yO) phase to the final LNO product by AC-STEM, EELS, and PED techniques. Due to the precursor's beam sensitivity, the sample is studied under low-dose imaging conditions. We observe defects such as pores, edge dislocations, lattice widening (increase in interlayer spacing), stacking faults,

and antiphase boundaries (APB) at the atomic level. Finally, using AC-STEM, EELS, and PED, we further demonstrate the phase evolution (ex situ) of the layered Ni(OH)₂ via the NiO-type phase to the layered LNO structure.

2. Results and Discussion

2.1. Investigation of the Ni(OH)₂ Precursor with High Spatial Resolution

To date, only conventional electron microscopy imaging techniques have been used to characterize Ni(OH)₂ compounds.^[10,31–34] The structural stability issues under the e-beam make the analysis nontrivial and the resulting structural studies challenging. Multiple reports suggest Ni(OH)₂ exhibiting a platelet-like morphology, although this can be tailored by the choice of precipitation parameters.^[10,31–34] In order to characterize the local defects in Ni(OH)₂, Ni_{1-y}Li_yO, and LNO, it is pivotal to understand their ideal crystal structures and how they are related. The structure of Ni(OH)₂ is described as a hexagonal close-packed structure of hydroxyl ions with a space group of $P\bar{3}m1$ ($a = 3.127$ Å, $c = 4.606$ Å) where Ni is placed on the 1a site (cell origin) and O, H on the 2d site.^[11] The Ni²⁺ ions are octahedrally coordinated by OH groups, which are then arranged in triangular nets via edge-sharing along the (001)_{trigonal} plane. Thus, it is isostructural to the mineral brucite and the layer-to-layer distance corresponds to the lattice parameter c ($d_{\text{stack}}[\text{Ni}(\text{OH})_2] = 4.606$ Å). The stacking sequence of the oxide anions layers can be described as an ABAB sequence with H⁺ in the tetrahedral site.^[35,36]

Figure 1 shows a HR HAADF micrograph of a Ni(OH)₂ platelet (≈ 10 nm in width) exhibiting the pristine layered Ni(OH)₂ structure. As can be seen from the area marked by a black arrow, the grain boundary region shows a surface reconstruction layer with a thickness of less than 1 nm. This Ni-rich layer is similar to the disordered rock salt-type phase that has already been observed at the grain boundaries of Ni-rich CAMs.^[37–39] The following section shows detailed structural analyses of imperfections at the atomic scale by employing a low-dose AC-STEM technique.

2.2. Probing the Defects in the Ni(OH)₂ Precursor

To date, various diffraction studies have been undertaken to understand the structural imperfections in the precursor materials. Due to the small crystallite size and relatively low crystallinity, a large number of microstructural variables might not have a one-to-one correlation with the peak profile features, making complete characterization a complex task. Thus, apart from anisotropic size effects, additional features like defects contribute to the XRD peak profile features.^[40–42] Wronski et al.,^[43] Delmas et al.,^[44] and Deabate et al.^[45] attributed the irregularities in the XRD line broadening to the presence of stacking faults and micro-distortions in the lattice structure. The defective surfaces can also arise from proton and hydroxide ion defects close to the crystalline surfaces.^[11,12,14] Hence, a comprehensive picture of microstructural evolution combined with a direct physical interpretation is lacking.

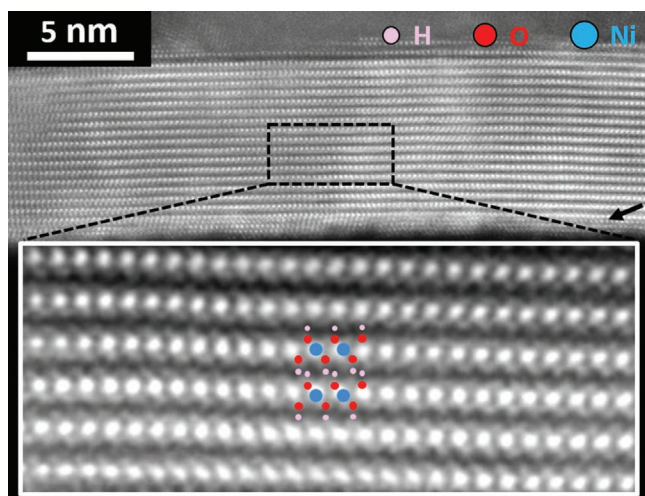


Figure 1. AC-STEM (HAADF) micrograph of the $\text{Ni}(\text{OH})_2$ precursor in [100] zone axis. The bottom inset is an atomically resolved image taken from the region marked with a black dashed rectangle indicating H (in pink), O (in red), and Ni (in blue). The black arrow points to the surface reconstruction layer at the grain boundary region. Please note that the size of the colored dots corresponds to the electron density, not to the size of the ions. The area of interest from where the data is collected is marked in Figure S7, Supporting Information.

As seen from **Figure 2a,b**, the AC-STEM micrographs demonstrate irregular pit-like structures marked by black arrows (please also refer to Figures S2 and S3, Supporting Information). Intriguingly, **Figure 2b** illustrates lattice expansion along the *c*-axis, with edge dislocations marked by an orange double arrow and yellow arrows, respectively. The lower contrast in the area of the expanded lattice suggests the presence of light element impurities trapped within the layers, such as water, sulfates, or carbonates. Interestingly, indeed sulfur (S) is detected by energy-dispersive X-ray spectroscopy, as shown in **Figure S4**, Supporting Information. Nonetheless, obtaining

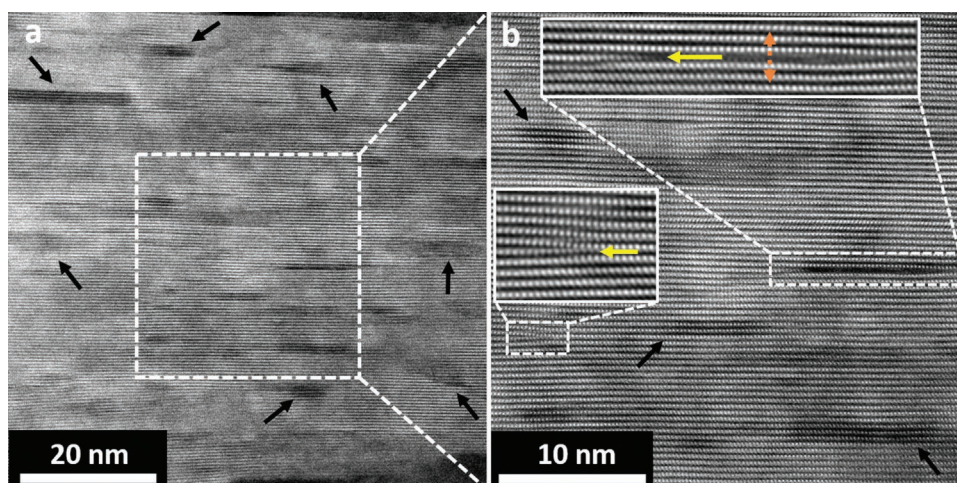


Figure 2. a) HAADF micrograph of the $\text{Ni}(\text{OH})_2$ precursor showing pores (marked with black arrows). b) A magnified image from the white dotted region in (a) indicating pores (black arrows), and edge dislocations (yellow arrows) with lattice widening (orange double arrow). The insets in (b) are atomically resolved images from the regions marked with white dashed rectangles. The area of interest shown in (a) is marked in Figure S2, Supporting Information.

spectral information at high-spatial resolution in a dose limited sample poses a challenge. Further work needs to be done to identify the chemical species trapped in the defective regions. These impurities presumably originate from the synthesis when nickel sulfate is used as a precursor in the precipitation of nickel hydroxide.^[37,46,47]

The HR images of the $\text{Ni}(\text{OH})_2$ precursor reveal a high density of various defects (especially as compared to the LNO CAM, as can be seen in **Figure 6**). The crystal imperfections in **Figure 3** can be identified as pores (black arrow), local lattice widening (orange double arrows), and dislocations or line defects (yellow arrows). Apart from these defects, the inset marked by a red square illustrates crystalline defects along the layered direction of $\text{Ni}(\text{OH})_2$ compared to the region marked by a blue square. The insets demonstrate a deformed unit cell (marked by an orange square) compared to the pristine layered $\text{Ni}(\text{OH})_2$ structure shown by a green square in **Figure 3**. This indicates that the layered precursor is engraved with stacking faults and APB defects (encircled by white dotted regions) that might go undetected otherwise because of their diffuse contrast.

2.3. Tracking Structural Evolution during LiNiO_2 Synthesis (Ex Situ)

The physicochemical properties of solids depend crucially on their microstructure. Crystallite size and imperfections in the crystal structure of the precursor can play a role during the synthesis of the layered oxide, which can further affect the material performance. In this section, we will track the LNO synthesis (ex situ) in three steps. First, starting from the pure $\text{Ni}(\text{OH})_2$ precursor, followed by the pre-annealed mixture of $\text{Ni}(\text{OH})_2$ particles with $\text{LiOH} \cdot \text{H}_2\text{O}$ at 350 °C, and finally the LNO CAM.

At the industrial scale, precipitation of metal hydroxides is the method of choice due to its scalability to achieve high

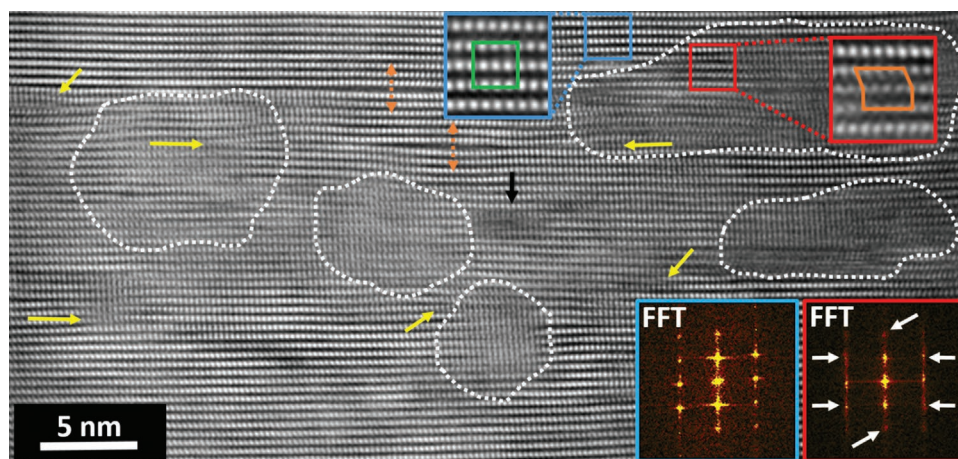


Figure 3. AC-STEM (HAADF) of the $\text{Ni}(\text{OH})_2$ precursor micrograph showing a highly defective region with edge-dislocations (yellow arrows), lattice widening (orange double arrows), diffuse contrast (white dotted regions) containing stacking faults, and APB defects. The insets are magnified images of a perfect layered structure of $\text{Ni}(\text{OH})_2$ (blue square) and a layered structure with a stacking fault (red square), respectively. The corresponding FFT's are shown as an inset where the stacking fault region exhibits smeared reflections marked by the white arrows. The area of interest from where the data is collected is marked in Figure S3, Supporting Information.

production volumes.^[12,44] Upon the reaction of $\text{Ni}(\text{OH})_2$ with LiOH starting at intermediate temperatures of 250–300 °C,^[6] the layered $\text{Ni}(\text{OH})_2$ compound dehydrates and the structure condenses. In the newly formed, rock salt-type $\text{Ni}_{1-\gamma}\text{Li}_\gamma\text{O}$ with $\gamma \leq 0.38$, the structure is described by the space group $Fm\bar{3}m$, where the metals statistically occupy the 4a site and the oxide anions reside on the 4b site. While the triangular motif of $(\text{Ni},\text{Li})\text{O}_6$ octahedra is not lost, the layer-to-layer stacking distance along the $[111]_{\text{cubic}}$ direction is halved to 2.386 Å due

to the migration of metals into the layer that was previously occupied by H in $\text{Ni}(\text{OH})_2$. Yet, when $d_{\text{stackl}}[(\text{Ni},\text{Li})\text{O}]$ is doubled ($2d_{\text{stack}} = 4.773 \text{ \AA}$), one can see that even the partial incorporation of Li on the 4a site leads to an expansion of the normalized layer-to-layer distance when compared to $\text{Ni}(\text{OH})_2$. The Li incorporation also influences the lattice parameter a , which is 4.1344(2) Å in $\text{Ni}_{0.781(5)}\text{Li}_{0.219(5)}\text{O}$ and thus smaller than in stoichiometric NiO ($a = 4.1792(2) \text{ \AA}$). The stacking of the oxide layers changes to an ABC stacking sequence along the direction

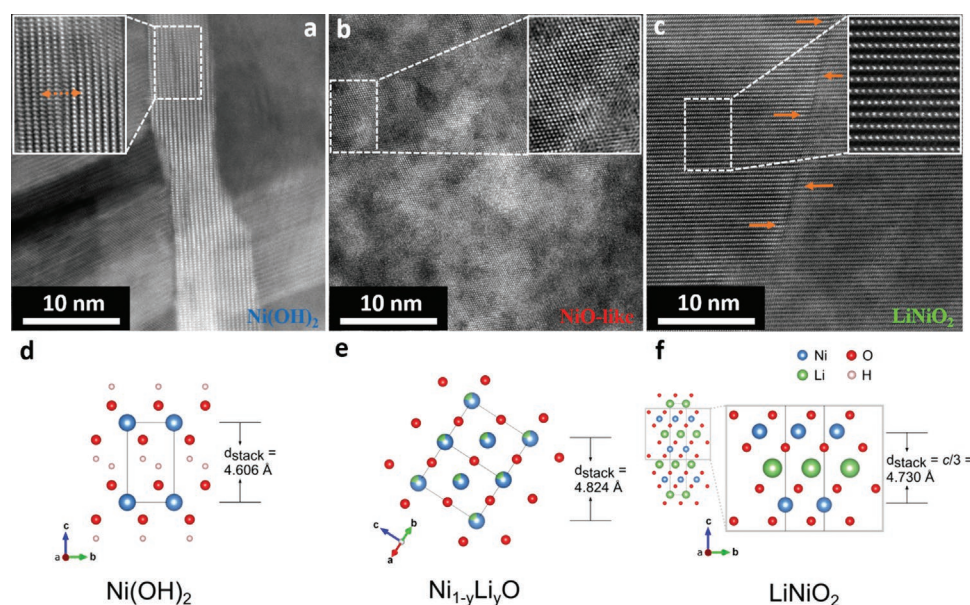


Figure 4. HAADF micrographs showing the structural evolution of $\text{Ni}(\text{OH})_2$ precursor (a) to pre-annealed $\text{Ni}_{1-\gamma}\text{Li}_\gamma\text{O}$ (NiO-like) phase (b) and the final LNO phase (also refer to the corresponding SEM images in Figure S1, Supporting Information). The insets shown are atomically resolved micrographs obtained from the regions marked with dotted white rectangles. The inset indicates lattice widening (a) marked with an orange double arrow, $\text{Ni}_{1-\gamma}\text{Li}_\gamma\text{O}$ (NiO-like) with nanodomains (b) and a regular LNO layered structure (c) with an intragranular domain interface (marked with orange arrows). The intragranular domain interface has a tilt boundary as the domain on the left is in the perfect zone axis and the domain on the right is slightly tilted. The figures (d–f) are respective crystal structure models of HR-STEM images (a–c).

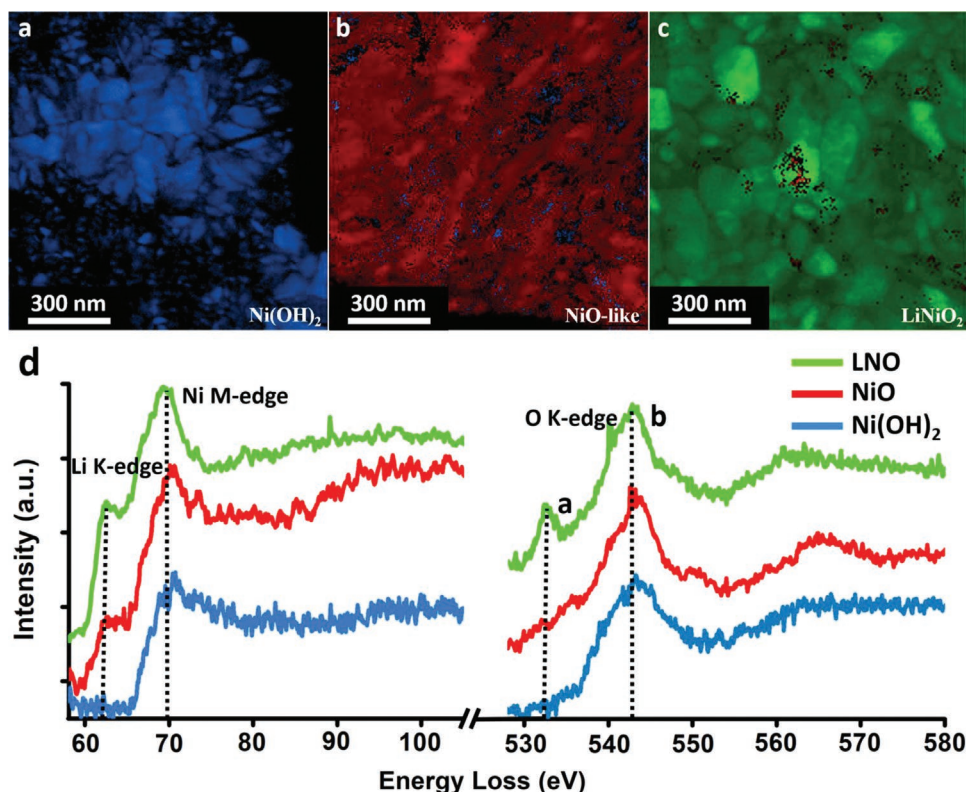


Figure 5. a–c) PED data showing the precursor evolution from a layered Ni(OH)₂ structure in blue (a) to rock salt-type Ni_{1-γ}Li_γO (NiO-like) in red (b) and finally to the layered LNO structure in green (c). We refer to the corresponding TEM images in Figure S8, Supporting Information. d) EELS spectrum showing the Li K-edge (≈62 eV), Ni M-edge (≈70 eV), and O K-edge, where the pre-edge peak of the O K-edge is marked as “a” (≈533 eV) and the main peak at ≈543 eV marked as “b.” We also refer to the Figure S9, Supporting Information.

[111]_{cubic} (please refer to Figure S5, Supporting Information). It is important to note that the intermediate compound is a solid solution. All compositions between $\gamma = 0$ and $\gamma = 0.38$ (Ni_{1-γ}Li_γO) can be formed during high temperature synthesis, with lattice parameters that continuously decrease with increasing γ . This makes the characterization process nontrivial. In the presence of Li excess beyond $\gamma > 0.38$ and in an oxygen atmosphere at temperatures beyond ≈500 °C, Ni²⁺ in Ni_{1-γ}Li_γO is further oxidized to Ni³⁺, inducing a rhombohedral distortion of the cubic lattice, toward a layered phase of stoichiometry Li_{1-2z}Ni_{1+2z}O₂. The new phase crystallizes in the space group $R\bar{3}m$, with three LNO layers per unit cell and approximate lattice parameters of $a = 2.9$ Å and $c = 14.4$ Å as reported in a very early publication.^[6,48]

In the HR-STEM images displayed in Figure 4, one observes the transformation of the layered structure of Ni(OH)₂ precursor (Figure 4a) into a rock salt-type NiO phase (Figure 4b) in the pre-annealed sample. The PED results further confirm the layered Ni(OH)₂ and the rock salt-type NiO phase (shown by blue and red colors in Figures 5a,b, respectively). The NiO phase shows a nanoparticulate morphology of tens of nm typical size confirmed from the STEM images in Figures S6 and S7, Supporting Information. By employing AC-STEM (Figure 4a–c) and PED (Figure 5a–c) methods, we confirm the structural transformation from the layered Ni(OH)₂ to rock salt-type NiO (Ni_{1-γ}Li_γO) and back to the lithium intercalated layered structure (LNO).

The lattice parameters strongly correlate with the presence and concentration of the antisite defect of Ni on the Li site, quantified by z . The phase transition can be described as a disorder-to-order transition, wherein the Li and Ni migrate from their shared site (Wyckoff position 4a in the cubic phase) to two separate sites for Li (Wyckoff position 3a) and Ni (Wyckoff position 3b) in two separate layers of different height.

To further investigate this structural transformation, EELS was employed. Here, the ionization edges can be interpreted by analyzing the energy loss of incident electrons due to excitations of electrons to unoccupied energy levels in the conduction band. In situ XRD studies prove that the NiO phase (Ni_{1-γ}Li_γO) already contains lithium after pre-annealing.^[6] We verify the Li content in the pre-annealed mixture of the rock salt-type NiO phase, as can be seen from the presence of the Li K-edge, the red plot in Figure 5d. We also refer to the EELS spectrum showing the Ni L_{2,3}-edges (also refer to the Figure S9, Supporting Information). Wherein we see a clear shift in the Ni L-edge from ≈854 to ≈860 eV during the transition from NiO-like to LNO phase, respectively. Similar peak shifts have been reported while comparing the cycled and surface degraded regions to the bulk regions, respectively, in Ni-based lithium transition metal oxides.^[49,50]

Moreover, the change in the shape of the O K-edge energy loss near edge structure fingerprint is susceptible to the local coordination around the O atom. The main peak (≈543 eV) as seen in Figure 5b arises from the excitation of electrons from

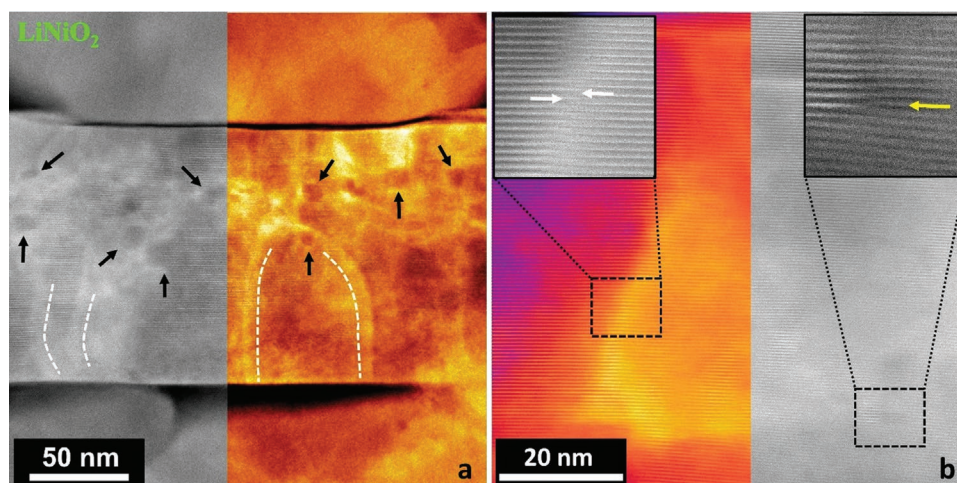


Figure 6. HAADF micrographs of the end product in the LNO synthesis (half false-colored). a) A primary grain having nanopore defects (marked by black arrows) and channel formation^[37] (marked by white dotted lines). b) A region with diffuse contrast comprising of an antiphase boundary (marked by white arrows) and an edge-dislocation (marked by yellow arrow). As a comparison to the commercial NiO precursor, we also refer to the Figure S10, Supporting Information.

the O 1s state to the unoccupied O 2p state, whereas the pre-peak (≈ 533 eV) can arise when the O 2p states hybridized with Ni 3d states. The pre-peak presence in LNO is a positive indication of the sharing of hole states (created at the O 2p level) with the NiO₆ unit, further confirming the presence of the layered LNO structure.^[51–53]

2.4. Origin of Structural Defects and Their Role during Lithiation

Achieving precise control over the layered LNO composition and structure is a complex task.^[6,54–57] As proven by AC-STEM imaging (Figures 2 and 3), the Ni(OH)₂ precursor is also imperfect, leading to the issues stated above. This section will endeavor to identify the probable origin of defects and their role during the synthesis process.

A few previous reports investigated the effect of the structural defects in Ni(OH)₂ on the electrochemical reactivity.^[58–61] The present understanding supports the fact that defects seen in the precursor depend on the kinetics of the precipitation process. The density of defects can be controlled by a very wide space of parameters that determine the supersaturation of the various hydroxide species in solution and therefore the kinetics of nucleation and growth. These parameters include pH, temperature, concentration of species in solution and of chelating agents, and stirring speed in the reactor. In general, it is believed that fast nucleation and growth lead to impurity trapping and interface formation during precipitation and hence are found to be critical.^[61–64] This was also applied to the other precursor variants containing Mn and Co. The Mn²⁺ cations are expected to easily oxidize to Mn³⁺ cations, resulting in different hydroxide phases. Incorporation of Co and Mn into the hexagonal Ni(OH)₂ crystal structure hence may create more disorder and defects.^[13,61,65,66]

The observation of defects such as stacking faults and local lattice widening due to trapping impurities have been reported previously by analyzing the X-ray patterns and infrared

spectroscopy. Bernard et al.,^[58] Faure et al.,^[59] McEwen,^[60] and Bette et al.^[61] reported intercalation of impurities between the Ni(OH)₂ slabs, like, for example, SO₄²⁻ ions, carbonate anions, and H₂O molecules, resulting in a local increase in the inter-layer spacing along the *c* axis. As seen from Figures 2b and 3, we can verify these reports by direct observation of lattice widening and stacking faults. Furthermore, in Figures 2 and 3 (also refer to Figure S2, Supporting Information), pores marked by black arrows manifest similarly to the nanopores in LNO (marked by black arrows in Figure 6a). The oxygen gas evolution is usually reported to be the cause of nanopore defects in the Ni-rich layered oxides CAMs.^[37,67,68] Nevertheless, there are no nanopore defects yet been reported in the Ni(OH)₂ precursor and further work needs to be carried out in order to get further insights into the nanopores formation mechanism. The role of intragranular nanopores in Ni-rich layered oxides CAMs was recently published discussing its impact on the capacity fade.^[37] The edge dislocations marked in the Ni(OH)₂ precursor (yellow arrows) in Figures 2b and 3 (also refer to Figures S2c and S3, Supporting Information) also appear in the LNO as shown in Figure 6b marked by the yellow arrow. Also, APBs observed in the precursor sample (indicated by white dotted regions in Figure 3) are seen in the LNO, as marked by the white arrows in Figure 6b. The role of precursor defects for the microstructure of the final LNO product is further confirmed by analyzing LNO synthesized from a commercial NiO precursor (refer to Figure S10, Supporting Information). Here, the primary grains did not show any pore defects, APBs, line defects, or channel formations.^[27,37]

This is in stark contrast to the observation of a significant number of pores, stacking faults, APBs, line defects, and local lattice widenings in the Ni(OH)₂ precursor compared to the final LNO product. Some defects, such as the locally widened lattice, seem to heal during thermal firing process and are not observed in LNO.^[69] Since there is a 2D to 3D to 2D transition during the LNO synthesis process from Ni(OH)₂ via Ni_{1-y}Li_yO to LNO, respectively, there is no direct transfer of defects

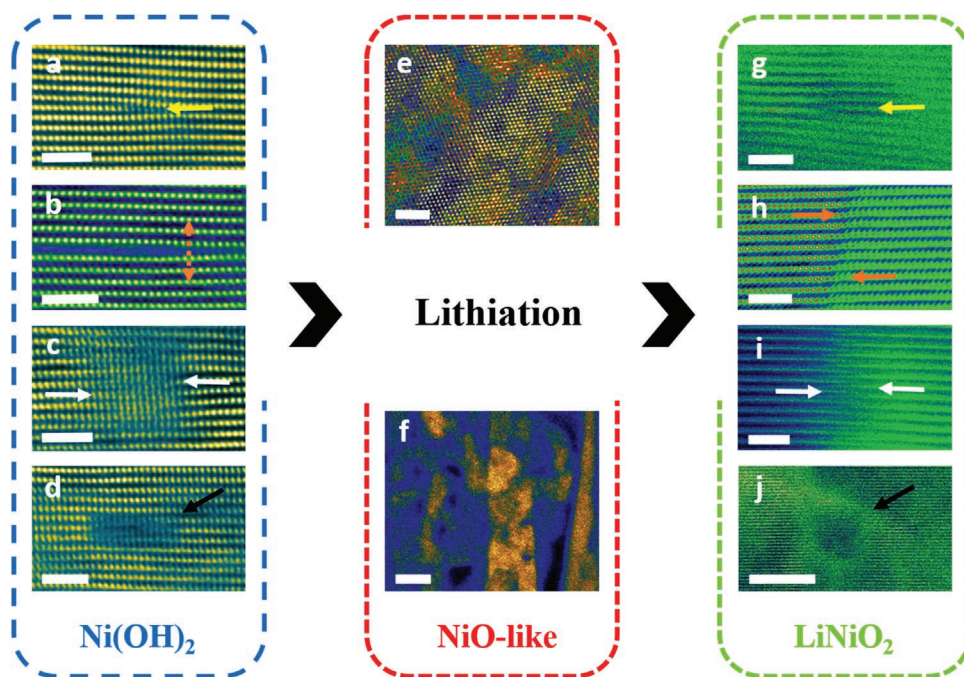


Figure 7. STEM micrographs (false-colored) of common defects observed in $\text{Ni}(\text{OH})_2$, $\text{Ni}_{1-y}\text{Li}_y\text{O}$ (NiO-like) phase, and LiNiO_2 CAM, respectively. The yellow arrows mark the line defects in (a,g). An orange double arrow in (b) represents lattice widening, whereas the orange arrows in (h) mark the intragranular domain interface. (c,i) show the presence of APB's. Black arrows mark pore formation in (d,j). $\text{Ni}_{1-y}\text{Li}_y\text{O}$ phase seen in (f) demonstrates nanoparticulate morphology having diffuse interface nanodomains (HR image in [e]). Scale bar: 2 nm (a–d,e,g–i), 20 nm (f), and 10 nm (j).

observed in $\text{Ni}(\text{OH})_2$ to LNO (refer to **Figure 7**). However, we see direct evidence of impurity trapping in $\text{Ni}(\text{OH})_2$ (refer to Figure 2 and Figures S2–S4, Supporting Information), which results in highly defective regions. The presence of highly defective regions may result in inhomogeneous lithiation during the synthesis process.

Moreover, due to the coexistence of multiple dislocations, stress gradients can occur. The experimental observation shows that the dislocations formed in the $\text{Ni}(\text{OH})_2$ precursor are parallel to the direction of the layers. However, edge dislocations can produce vertical and parallel displacements to the extra half-plane, making the investigation more challenging and disrupting the stacking sequence.^[68,70] Due to the proximity of the defects, attractive or repulsive forces tend to reduce the total elastic energy, which is also direction- and location-dependent.^[71–73] In the interim stage of lithium intercalation, lithium may diffuse faster along the dislocation and spread inhomogeneously.^[70] Thus, apart from the dislocations adverse effect, the dislocation cores may create fast Li transport channels.^[74,75] Hence, the presence of dislocations may either be beneficial or detrimental to the lithiation process.^[26,67,70,71,76]

It is essential to note that there are no studies reported on the role of structural defects during the synthesis process when $\text{Ni}(\text{OH})_2$ is lithiated. Due to the crystal formation conditions, the thermal movement of atoms, and other factors, the arrangement of atoms often has regions that deviate from the ideal crystal structure. Thus, the evolution of stacking faults and other defects is not trivial and more work needs to be done in different zone axis to investigate any additional defect propagation directions. Further in situ S/TEM investigation can improve our understanding of the defect dynamics during the synthesis process.

3. Conclusion

We comprehensively investigated the dose-sensitive $\text{Ni}(\text{OH})_2$ precursor and its structural evolution during the synthesis process (ex situ) at high-spatial resolution with state-of-the-art electron microscopic techniques. The samples were obtained from an industrially relevant precipitation method. Employing a low-dose AC-STEM technique has enabled us to access the structural transformation at high spatial resolution. We see the presence of highly defective regions in $\text{Ni}(\text{OH})_2$, comprising pores, local lattice widening, edge dislocations, stacking faults, and APBs. We traced the structural transformation at the atomic and micron scales by combining the STEM, EELS, and PED results. Having access to all types of defects is crucial as global averaging methods (such as PXRD) can only analytically work on a specific type of defect identification.

The LNO synthesis from hydroxide precursors is found to be an intricate process involving the collapse of the layered $\text{Ni}(\text{OH})_2$ nanoplatelet structure to a nanoparticulate rock salt-type phase ($\text{Ni}_{1-y}\text{Li}_y\text{O}$). The EELS measurements confirm that the nanoparticulate NiO contains lithium. The defects observed and widely reported in CAMs are likely to arise, or at least to be exacerbated, by the inherent defects present in the $\text{Ni}(\text{OH})_2$ precursor. Nonetheless, the defect dynamics during the lithium intercalation will need further investigation. The origin of defects in the $\text{Ni}(\text{OH})_2$ precursor can be traced back to the precipitation step. While our in-depth investigation shows the variety of structural defects in $\text{Ni}(\text{OH})_2$, which also are found in final LNO product, it is yet unclear how these defects are “transmitted” during the intermediate occurrence of the cubic rock salt-type phase. Finally, these findings provide new insights into the CAM

synthesis steps, with deeper understanding and calls for further studies, tracing individual structural defects.

4. Experimental Section

Synthesis of the Ni(OH)₂ Precursor, Pre-Annealed NiO, and LNO: The synthesis was described in the literature.^[77] Ni(OH)₂ (*D*₅₀ = 11.8 μm, BASF SE, Germany) was a commercial, battery grade product and used as received. In order to obtain NiO and LNO, 1 eq. Ni(OH)₂ and 1.01 eq. LiOH·H₂O (BASF SE, Germany) were mixed using a laboratory blender for 30 min under an Ar atmosphere. To obtain the pre-annealed product NiO, the mixture was heated to in an alumina crucible under an O₂ flow of 2 volume exchanges per hour in a tube furnace (Nabertherm P330) with heating and cooling ramps of 3 K min⁻¹. The maximum temperature of 350 °C was kept for 12 h. For the final product LNO, the Ni(OH)₂ and LiOH reactant mixture was annealed at 500 °C for 12 h followed by a final annealing at 700 °C for 6 h.

The synthesis of LNO from commercial NiO precursor, shown in Figure 6 is described in ref. [27].

Sample Preparation: The S/TEM sample preparation and SEM imaging was carried out with a JEOL JIB 4601F multibeam system operating at 1–30 kV for the electron and Ga-ion beam. To minimize air exposure, all the samples were stored in a glove box. The secondary particles of Ni(OH)₂ precursor, pre-annealed NiO, and LNO were first sputter-coated by carbon (≈40 nm) using a Leica EM ACE600 sputtering system. Further coating was accomplished using an e-beam assisted C/W deposition, followed by Ga-ion-assisted 3 μm thick W deposition. Starting with a 30 kV ion beam, a cross-sectional sample was fabricated by thinning down the lamella to a thickness under ≈100 nm, where a 3 kV ion beam does the polishing. Finally, low-energy gentle milling (Fishione Model 1040 Nanomill) was performed using a 500 eV Ar-ion beam on both sides.

Material Characterization: AC-STEM micrographs were obtained by a double Cs-corrected JEOL JEM-2200 FS equipped with an in-column omega filter operated at 200 kV with a 15 mrad convergence angle. All the STEM micrographs were HAADF images taken by setting the annular dark-field detector's inner and outer angle to 70 and 280 mrad, respectively, with a beam current of ≈1.2 pA. To further reduce the e-beam influence, several individual fast image acquisitions were undertaken and aligned by the Smart Align script.^[78] This resulted in restricting the total dose to ≈1000 eÅ⁻². EELS data and the image analysis were carried out using the Gatan Digital Micrograph and ImageJ software. The insets in Figures 1–4 in the manuscript and Figures S2 and S3, Supporting Information, are ABSF filtered micrographs.^[79] The inset structure models (Figure 1 and Figure S8, Supporting Information) were obtained from the VESTA software.^[80] The Ni(OH)₂, NiO, and LNO phase maps were obtained with a JEOL JEM-3010 300 kV LaB₆ cathode filament equipped with an automated crystal orientation mapping system from NanoMEGAS. The PED patterns were obtained with the lowest e-beam dose possible of ≈20 e Å⁻² s⁻¹ by using the smallest condenser aperture at spot size 5. Figure 5 displays dark areas representing low-reliability regions. In addition, Figure 5b,c shows certain patches of the layered Ni(OH)₂ (in blue) and the NiO rock-salt (in red) phases, respectively. The spatial resolution and phase identification reliability were limited by the sample morphology, electron gun-type, spherical aberration (Cs), beam diameter (≈10 nm), and the precession angle (≈0.6°).

Supporting Information

Supporting Information is available from the Wiley Online Library or from the author.

Acknowledgements

The authors gratefully acknowledge support from the Bundesministerium für Bildung und Forschung (BMBF) in the framework of the FestBatt

cluster of competence (Projects 03XP0176C and 03XP0176D), as well by BASF SE (Ludwigshafen, Germany).

Open access funding enabled and organized by Projekt DEAL.

Conflict of Interest

The authors declare no conflict of interest.

Data Availability Statement

The data that support the findings of this study are available from the corresponding author upon reasonable request.

Keywords

aberration-corrected scanning transmission electron microscopy, antiphase boundaries, defects, dislocations, e-dose reduction, electron energy loss spectroscopy, FIB, lattice widening, Li-ion battery, pores, Li-ion batteries, LiNiO₂ precursor

Received: September 6, 2022

Revised: October 17, 2022

Published online: November 26, 2022

- [1] T. Liu, L. Yu, J. Liu, J. Lu, X. Bi, A. Dai, M. Li, M. Li, Z. Hu, L. Ma, D. Luo, J. Zheng, T. Wu, Y. Ren, J. Wen, F. Pan, K. Amine, *Nat. Energy* **2021**, *6*, 277.
- [2] S. Neudeck, F. Walther, T. Bergfeldt, C. Suchomski, M. Rohnke, P. Hartmann, J. Janek, T. Brezesinski, *ACS Appl. Mater. Interfaces* **2018**, *10*, 20487.
- [3] K. Ghatak, S. Basu, T. Das, V. Sharma, H. Kumar, D. Datta, *Phys. Chem. Chem. Phys.* **2018**, *20*, 22805.
- [4] H. Li, M. Cormier, N. Zhang, J. Inglis, J. Li, J. R. Dahn, *J. Electrochem. Soc.* **2019**, *166*, A429.
- [5] M. Bianchini, M. Roca-Ayats, P. Hartmann, T. Brezesinski, J. Janek, *Angew. Chem.* **2018**, *58*, 10542.
- [6] M. Bianchini, F. Fauth, P. Hartmann, T. Brezesinski, J. Janek, *J. Mater. Chem. A* **2020**, *8*, 1808.
- [7] J. B. Goodenough, D. G. Wickham, W. J. Croft, *J. Phys. Chem. Solids* **1958**, *5*, 107.
- [8] E. Antolini, *Mater. Chem. Phys.* **2003**, *82*, 937.
- [9] P. Kalyani, N. Kalaiselvi, *Sci. Technol. Adv. Mater.* **2005**, *6*, 689.
- [10] G.-X. Tong, F.-T. Liu, W.-H. Wu, J.-P. Shen, X. Hu, Y. Liang, *CrystEngComm* **2012**, *14*, 5963.
- [11] C. Greaves, M. A. Thomas, *Acta Crystallogr., Sect. B: Struct. Sci.* **1986**, *42*, 51.
- [12] M. C. Bernard, R. Cortes, M. Keddad, H. Takenouti, P. Bernard, S. Senyari, *J. Power Sources* **1996**, *63*, 247.
- [13] F. Zhou, X. Zhao, A. van Bommel, A. W. Rowe, J. R. Dahn, *Chem. Mater.* **2010**, *22*, 1015.
- [14] D. S. Hall, D. J. Lockwood, C. Bock, B. R. MacDougall, *Proc. R. Soc. A* **2015**, *471*, 20140792.
- [15] J. McBreen, in *Handbook of Battery Materials*, John Wiley & Sons, Ltd., New York, **2011**, pp. 149–168.
- [16] S. L. Bihan, M. Figlarz, *J. Cryst. Growth* **1972**, *13–14*, 458.
- [17] S. I. Cordoba-Torresi, C. Gabrielli, A. H.-L. Goff, R. Torresi, *J. Electrochem. Soc.* **1991**, *138*, 1548.
- [18] Y. Zhu, C. Cao, S. Tao, W. Chu, Z. Wu, Y. Li, *Sci. Rep.* **2014**, *4*, 5787.
- [19] J. Maier, *Angew. Chem., Int. Ed. Engl.* **1993**, *32*, 313.

- [20] J. Maier, *Angew. Chem., Int. Ed. Engl.* **1993**, *32*, 528.
- [21] L. de Biasi, A. Schiele, M. Roca-Ayats, G. Garcia, T. Brezesinski, P. Hartmann, J. Janek, *ChemSusChem* **2019**, *12*, 2240.
- [22] C. S. Yoon, D.-W. Jun, S.-T. Myung, Y.-K. Sun, *ACS Energy Lett.* **2017**, *2*, 1150.
- [23] S. Muto, Y. Sasano, K. Tatsumi, T. Sasaki, K. Horibuchi, Y. Takeuchi, Y. Ukyo, *J. Electrochem. Soc.* **2009**, *7*.
- [24] Y. Bi, J. Tao, Y. Wu, L. Li, Y. Xu, E. Hu, B. Wu, J. Hu, C. Wang, J.-G. Zhang, Y. Qi, J. Xiao, *Science* **2020**, *370*, 1313.
- [25] S. Li, Z. Yao, J. Zheng, M. Fu, J. Cen, S. Hwang, H. Jin, A. Orlov, L. Gu, S. Wang, Z. Chen, D. Su, *Angew. Chem., Int. Ed.* **2020**, *59*, 22092.
- [26] P. Yan, J. Zheng, M. Gu, J. Xiao, J.-G. Zhang, C.-M. Wang, *Nat. Commun.* **2017**, *8*, 14101.
- [27] S. Ahmed, M. Bianchini, A. Pokle, M. S. Munde, P. Hartmann, T. Brezesinski, A. Beyer, J. Janek, K. Volz, *Adv. Energy Mater.* **2020**, *10*, 2001026.
- [28] P. D. Nellist, in *Scanning Transmission Electron Microscopy* (Eds: S. J. Pennycook, P. D. Nellist), Springer, New York **2011**, pp. 91–115.
- [29] P. D. Nellist, S. J. Pennycook, in *Advances in Imaging and Electron Physics* (Ed: P. W. Hawkes), Elsevier, New York **2000**, pp. 147–203.
- [30] P. A. Midgley, A. S. Eggeman, *IUCr* **2015**, *2*, 126.
- [31] M. Casas-Cabanas, M. R. Palacín, J. Rodríguez-Carvajal, *Powder Diffr.* **2005**, *20*, 334.
- [32] S. Ni, X. Lv, T. Li, X. Yang, L. Zhang, *J. Mater. Chem. A* **2013**, *1*, 1544.
- [33] D. Zheng, M. Li, Y. Li, C. Qin, Y. Wang, Z. Wang, *Beilstein J. Nanotechnol.* **2019**, *10*, 281.
- [34] T. Nguyen, M. Boudard, M. J. Carmezim, M. F. Montemor, *Sci. Rep.* **2017**, *7*, 39980.
- [35] C. Greaves, M. A. Thomas, *Acta Crystallogr.* **1986**, *42*, 51.
- [36] M. Casas-Cabanas, M. D. Radin, J. Kim, C. P. Grey, A. V. der Ven, M. R. Palacín, *J. Mater. Chem. A* **2018**, *6*, 19256.
- [37] S. Ahmed, A. Pokle, S. Schweidler, A. Beyer, M. Bianchini, F. Walther, A. Mazilkin, P. Hartmann, T. Brezesinski, J. Janek, K. Volz, *ACS Nano* **2019**, *13*, 10694.
- [38] J. Xu, F. Lin, M. M. Doeff, W. Tong, *J. Mater. Chem. A* **2017**, *5*, 874.
- [39] A. Pokle, S. Ahmed, S. Schweidler, M. Bianchini, T. Brezesinski, A. Beyer, J. Janek, K. Volz, *ACS Appl. Mater. Interfaces* **2020**, *12*, 57047.
- [40] A. R. Stokes, *Proc. Phys. Soc.* **1948**, *61*, 382.
- [41] D. Louër, D. Weigel, J. I. Langford, *J. Appl. Crystallogr.* **1972**, *5*, 353.
- [42] L. Lutterotti, P. Scardi, P. Maistrelli, *J. Appl. Crystallogr.* **1992**, *25*, 459.
- [43] Z. S. Wronski, G. J. C. Carpenter, P. J. Kalal, *Proceedings of the Symposium on Exploratory Research and Development of Batteries for Electric and Hybrid Vehicles*, (Eds: W. A. Adams, A. R. Landgrebe, B. Scrosati), The Electrochemical Society, Pennington, NJ **1996**, p. 177.
- [44] C. Delmas, C. Tessier, *J. Mater. Chem.* **1997**, *7*, 1439.
- [45] S. Deabate, F. Forgeot, F. Henn, *J. Power Sources* **2000**, *87*, 125.
- [46] T. Zeng, C. Zhang, *J. Mater. Sci.* **2020**, *55*, 11535.
- [47] A. Savina, E. Orlova, A. Morozov, S. Luchkin, A. Abakumov, *Nanomaterials* **2020**, *10*, 2381.
- [48] L. D. Dyer, B. S. Borie, G. P. Smith, *J. Am. Chem. Soc.* **1954**, *76*, 1499.
- [49] S. Hwang, S. Y. Kim, K. Y. Chung, E. A. Stach, S. M. Kim, W. Chang, *APL Mater.* **2016**, *4*, 096105.
- [50] S. Zheng, R. Huang, Y. Makimura, Y. Ukyo, C. A. J. Fisher, T. Hirayama, Y. Ikuhara, *J. Electrochem. Soc.* **2011**, *158*, A357.
- [51] F. Lin, I. M. Markus, M. M. Doeff, H. L. Xin, *Sci. Rep.* **2014**, *4*, 5694.
- [52] F. Lin, D. Nordlund, I. M. Markus, T.-C. Weng, H. L. Xin, M. M. Doeff, *Energy Environ. Sci.* **2014**, *7*, 3077.
- [53] A. K. Shukla, Q. M. Ramasse, C. Ophus, H. Duncan, F. Hage, G. Chen, *Nat. Commun.* **2015**, *6*, 8711.
- [54] R. Weber, H. Li, W. Chen, C.-Y. Kim, K. Plucknett, J. R. Dahn, *J. Electrochem. Soc.* **2020**, *167*, 100501.
- [55] H. X. Yang, Q. F. Dong, X. H. Hu, X. P. Ai, S. X. Li, *J. Power Sources* **1999**, *79*, 256.
- [56] P. Kurzahls, F. Riewald, M. Bianchini, H. Sommer, H. A. Gasteiger, J. Janek, *J. Electrochem. Soc.* **2021**, *168*, 110518.
- [57] F. Riewald, P. Kurzahls, M. Bianchini, H. Sommer, J. Janek, H. A. Gasteiger, *J. Electrochem. Soc.* **2022**, *169*, 020529.
- [58] M. C. Bernard, P. Bernard, M. Keddad, S. Senyari, H. Takenouti, *Electrochim. Acta* **1996**, *41*, 91.
- [59] C. Faure, C. Delmas, M. Fouassier, *J. Power Sources* **1991**, *35*, 279.
- [60] R. S. McEwen, *J. Phys. Chem.* **1971**, *75*, 1782.
- [61] S. Bette, B. Hinrichsen, D. Pfister, R. E. Dinnebie, *J. Appl. Crystallogr.* **2020**, *53*, 76.
- [62] D. D. Edie, D. J. Kirwan, *Ind. Eng. Chem.* **1973**, *12*, 100.
- [63] J. M. Poate, J. Linnros, F. Priolo, D. C. Jacobson, J. L. Batstone, M. O. Thompson, *Phys. Rev. Lett.* **1988**, *60*, 1322.
- [64] G. H. Gilmer, *Mater. Sci. Eng., R* **1984**, *65*, 15.
- [65] L. Wang, K.-H. Young, H.-T. Shen, *Batteries* **2016**, *2*, 16.
- [66] R. Venkatkarthick, J. Niu, A. Srikaow, C. Sriprachubwong, S. Vasudevan, A. Tuantranont, J. Qin, *ACS Appl. Energy Mater.* **2021**, *4*, 6520.
- [67] P. Yan, J. Zheng, T. Chen, L. Luo, Y. Jiang, K. Wang, M. Sui, J.-G. Zhang, S. Zhang, C. Wang, *Nat. Commun.* **2018**, *9*, 2437.
- [68] S. Ahmed, A. Pokle, M. Bianchini, S. Schweidler, A. Beyer, T. Brezesinski, J. Janek, K. Volz, *Matter* **2021**, *4*, 3953.
- [69] S. Li, G. Qian, X. He, X. Huang, S.-J. Lee, Z. Jiang, Y. Yang, W.-N. Wang, D. Meng, C. Yu, J.-S. Lee, Y. S. Chu, Z.-F. Ma, P. Pianetta, J. Qiu, L. Li, K. Zhao, Y. Liu, *Nat. Commun.* **2022**, *13*, 704.
- [70] A. Ulvestad, A. Singer, J. N. Clark, H. M. Cho, J. W. Kim, R. Harder, J. Maser, Y. S. Meng, O. G. Shpyrko, *Science* **2015**, *348*, 1344.
- [71] H.-Y. S. Huang, Y.-X. Wang, *J. Electrochem. Soc.* **2012**, *159*, A815.
- [72] D. J. Bacon, D. M. Barnett, R. O. Scattergood, *Prog. Mater. Sci.* **1980**, *23*, 51.
- [73] P. Peyla, A. Vallat, C. Misbah, H. Müller-Krumbhaar, *Phys. Rev. Lett.* **1999**, *82*, 787.
- [74] M. Legros, G. Dehm, E. Arzt, T. J. Balk, *Science* **2008**, *319*, 1646.
- [75] C. Yan, G. Chen, J. Sun, C. Lv, J. Pei, *Nano Energy* **2015**, *15*, 558.
- [76] H. Wang, Y.-I. Jang, B. Huang, D. R. Sadoway, Y.-M. Chiang, *J. Electrochem. Soc.* **1999**, *146*, 473.
- [77] D. Weber, J. Lin, A. Pokle, K. Volz, J. Janek, T. Brezesinski, M. Bianchini, *J. Electrochem. Soc.* **2022**, *169*, 030540.
- [78] L. Jones, H. Yang, T. J. Pennycook, M. S. J. Marshall, S. V. Aert, N. D. Browning, M. R. Castell, P. D. Nellist, *Adv. Struct. Chem. Imaging* **2015**, *1*, 8.
- [79] R. Kilaas, *J. Microsc.* **1998**, *190*, 45.
- [80] K. Momma, F. Izumi, *J. Appl. Crystallogr.* **2011**, *44*, 1272.